Anodic Activation of Iron Corrosion in Clay Media under Water-Saturated Conditions at 90 °C: Characterization of the Corrosion Interface

5 AUTHORS, INCLUDING:

Michel Schlegel

Atomic Energy and Alternative Energies Co…

84 PUBLICATIONS   **2,034** CITATIONS

SEE PROFILE

cécile Blanc

Atomic Energy and Alternative Energies Co…

15 PUBLICATIONS   **102** CITATIONS

SEE PROFILE

Dimitri Prêt

Université de Poitiers

38 PUBLICATIONS   **357** CITATIONS

SEE PROFILE

Eddy Foy

Atomic Energy and Alternative Energies Co…

55 PUBLICATIONS   **556** CITATIONS

SEE PROFILE

Anodic Activation of Iron Corrosion in Clay Media under Water-Saturated Conditions at 90 °C: Characterization of the Corrosion Interface

MICHEL L. SCHLEGEL,*,†,‡
CHRISTIAN BATAILLON,§
CÉCILE BLANC,† DIMITRI PRET,‖ AND
EDDY FOY⊥

CEA, DEN, Laboratory for the Reactivity of Surfaces and Interfaces, Bât. 391, F91191 Gif-sur-Yvette, France, University of Evry, UMR 8587 LAMBE, F91025 Evry, France, CEA, DEN, Laboratory for the Study of Aqueous Corrosion, Bât. 458, F91191 Gif-sur-Yvette, France, University of Poitiers, FRE CNRS-INSU 3114 HydrASA, F86022 Poitiers, France, and CEA, DSM, IRaMis/SIS2M/LAPA, Bât. 637, F91191 Gif-sur-Yvette, France

To understand the process governing iron corrosion in clay over centuries, the chemical and mineralogical properties of solids formed by free or anodically activated corrosion of iron in water-saturated clay at 90 °C over 4 months were probed using microscopic and spectroscopic techniques. Free corrosion led to the formation of an internal discontinuous thin (<3 μm thick) magnetite layer, an external layer of Fe-rich phyllosilicate, and a clay transformation layer containing Ca-doped siderite (Ca$_{0.2}$Fe$_{0.8}$CO$_3$). The thickness of corroded iron equaled ~5–7 μm, consistent with previous studies. Anodic polarization resulted in unequally distributed corrosion, with some areas corrosion-free and others heavily corroded. Activated corrosion led to the formation of an inner magnetite layer, an intermediate Fe$_2$CO$_3$(OH)$_2$ (chukanovite) layer, an outer layer of Fe-rich 7 Å-phyllosilicate, and a transformed matrix layer containing siderite (FeCO$_3$). The corroded thickness was estimated to 85 μm, less than 30% of the value expected from the supplied anodic charge. The difference was accounted for by reoxidation at the anodically polarized surface of cathodically produced H$_2$(g). Thus, free or anodically activated corroding conditions led to structurally similar interfaces, indicating that anodic polarization can be used to probe the long-term corrosion of iron in clay. Finally, corrosion products retained only half of Fe oxidized by anodic activation. Missing Fe probably migrated in the clay, where it could interact with radionuclides released by alteration of nuclear glass.

---

* Corresponding author e-mail: Michel.Schlegel@cea.fr.
† CEA, DEN, Laboratory for the Reactivity of Surfaces and Interfaces.
‡ University of Evry.
§ CEA, DEN, Laboratory for the Study of Aqueous Corrosion.
‖ University of Poitiers.
⊥ CEA, DSM, IRaMis/SIS2M/LAPA.

1. Introduction

Electricity production by nuclear power plants has led to the accumulation of high-level radioactive waste (HLRW). Several countries are investigating geological disposal to confine HLRW for at least 10 000 years. According to current designs assessed in France (*1*), HLRW would be stored as nuclear glass in stainless steel containers and low-alloy steel overpacks. These overpacks would be surrounded by a backfill of bentonite, a clay material, or directly inserted in a Callovo-Oxfordian (COx) clay host rock. Water-saturated anoxic conditions and temperatures up to 90 °C resulting from radioactive decay will promote overpack and container corrosion and clay transformation, ultimately exposing glass to alteration (*2*). The rate of glass alteration could then be enhanced by sorption of glass-forming dissolved species (e.g., silicate) on corrosion products (*3*). However, the importance of these reactions can be estimated only if the nature and reactivity of corrosion products is known.

To better understand corrosion processes, integrated experiments were designed in which clay was contacted with metal iron under saturated conditions and temperatures up to 90 °C (*2, 4, 5*). In some experiments, the corrosion rate was measured by electrospectrometry (*6, 7*). In addition, the corrosion magnitude and the nature of corrosion products were investigated by microspectroscopic characterization of corroded interfaces (*8*). These investigations revealed the coexistence of corrosion layers of contrasted mineralogy. They also showed that, even at 90 °C and under saturated conditions, only 10 to 20 μm of metal iron is corroded after 1 year. Much longer corrosion times would be needed to obtain enough corrosion products to study their effect on glass alteration. To overcome this limitation, corrosion can be activated by anodic polarization, but the corrosion interface might then substantially differ from that obtained by free corrosion.

The goal of this study is to compare iron corrosion in clay under repository conditions for either a freely corroding probe (FCP) or an anodically polarized probe (APP). To this end, the FCP (a massive iron rod) and the APP (an iron microcontainer primarily meant to investigate the impact of corrosion products on glass alteration) were inserted together in a clay brick and reacted under water-saturated anoxic conditions at 90 °C for 4 months. Characterization of the corrosion interface for the FCP and APP revealed consistent trends in corrosion processes and shed light on long-term interactions between iron and clay in a nuclear waste repository.

2. Materials and Methods

The corrosion experiment followed a protocol adapted from previous studies (*7*) and detailed in the Supporting Information. Briefly, an argillite brick was shaped in COx clay. Three probes were inserted horizontally in the brick (Figure SI-1 in the Supporting Information). The lower probe was a gold electrode to measure the electrochemical potential of the brick, the upper probe a massive rod of ARMCO ferrite iron (38 mm long, 10 mm diameter), and the center probe a microcontainer, made by a SON68 (the inactive equivalent of R7T7 nuclear glass) glass rod (38 mm long, 10 mm diameter) sealed in a 400 μm thick tube of ARMCO ferrite iron. The clay brick was inserted in a confining cell, where it was purged with He to remove air, then saturated with COx synthetic porewater, and heated at 90 °C for 4 months. Corrosion of the microcontainer was activated by an anodic current corresponding to a corrosion rate of 105 μm/month, assuming
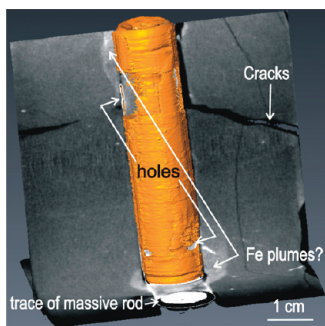
FIGURE 1. Microtomographical surface rendering (yellow) of the segmented iron envelope of the microcontainer combined with two perpendicular slices extracted of the reconstructed volume. This allows visualizing two corrosion "holes" (nearly fully corroded spots) close to the microcontainer extremities and iron migration halos in argillite.

oxidation of metal Fe to a valence of +II. The cathodic reaction (water reduction) was delocalized at the surface of the confining cell.

At the end of the corrosion period, the clay brick was extracted from the high-pressure setup and embedded in epoxy resin. The block was then analyzed by X-ray tomography on a Viscom X8050 equipped with a W X-ray source to nondestructively assess the corrosion damage with a spatial resolution of 86 μm (the size of the cubic voxel). Afterward, the block was cut perpendicular to the probe axes, and sections were polished to 1 μm roughness in an anoxic glovebox.

Optical microphotography and micro-Raman (μRaman) spectrometry were performed under anoxic conditions, with the sample heat-welded in a transparent polyethylene bag. Optical microphotographs were collected on a Leica MDRXA500 microscope and processed with the Leica software. Micro-Raman spectra were recorded at a laser wavelength of 532 nm with a HoloLab 5000 spectrometer mounted on an Olympus BX60 microscope. The laser power was kept to 500 μW over 3 × 3 μm^2 areas to avoid thermal degradation of Fe (hydr)oxides (9, 10). Scanning electron microscopy (SEM) was performed on a JEOL JSM7000-F equipped with a field emission gun and operated at 15 kV and a probe current of ~4 nA. Energy-dispersive X-ray (EDX) analysis was performed using a silicon drift detector (Oxford Instruments). X-ray Diffraction with a microbeam (μXRD) was performed on thin sections using a rotating anode source (Mo Kα radiation) focused to 30 × 50 μm^2 (vertical × horizontal). Diffraction patterns were collected in transmission mode with an image plate (GE Healthcare), then circularly integrated with FIT2D (11).

3. Results and Interpretation

3.1. X-ray Tomography. X-ray tomography revealed the presence of major cracks intersecting the whole brick, likely related to porewater bypasses formed during corrosion (Figure 1). The sharp limits of the microcontainer are evident in tomography, suggesting only partial corrosion. This was confirmed by segmenting the microcontainer using a 3D propagation algorithm selecting connected voxels having attenuation coefficients above a threshold value. The volume rendering of this segmented envelope visualized only voxels with X-ray attenuation coefficients significantly greater than those of the adjacent glass and clay, i.e., microcontainer walls with thickness >86 μm (the voxel size) (Figure 1). This revealed that corrosion was heterogeneously distributed over the microcontainer surface, with residual thickness thinner than 86 μm at each microcontainer end, possibly corresponding to holes. Halos with appreciable attenuation coefficients were detected in the surrounding argillite beneath these "holes"

and extended up to 6 mm from the APP surface. These halos may correspond to the diffusion of heavy elements in the clay matrix, likely oxidized Fe from the APP corrosion. Finally, it was impossible to obtain microtomographic evidence for corrosion near the FCP surface at the 86 μm resolution. On the basis of this tomographic information, the brick was cut and polished near one of the APP "holes" for further analysis.

3.2. Probe Characterization by Microscopic Techniques. *Freely Corroding Probe.* Optical images revealed little to no transformation of the clay contacting the FCP (Figure SI-2 in the Supporting Information). Detailed MEB characterization of the FCP−clay interface showed the presence of thin corrosion layers (Figure SI-3 in the Supporting Information). As previously observed (8, 12), this interface was made of a dense product layer (DPL) and a transformed matrix layer (TML). On images in backscattered electron (BSE) mode, the metal appeared very electron-dense (bright) and contacted a darker (less electron-dense) layer, with, sometimes, a middle fringe of intermediate electron density. The TML appeared to be massive in contact to the DPL and fuzzy toward the unaltered clay. This corrosion facies was reminiscent of that observed for a previous sample, where a thin internal DPL (iDPL) of magnetite (Fe_3O_4) was in contact with metal, and a Fe-phyllosilicate external DPL (eDPL) was present between the iDPL and a siderite-containing TML (8). Elemental maps confirmed this zoning, the middle fringe being the iDPL (Figure SI-3 in the Supporting Information). Point analysis of Fe-rich domains in the TML showed that O, Fe, and Ca predominated (68.1, 23.7, and 6.1 atomic %, respectively), with minor contributions from Mg, S, Al (all below 1.2 atomic %). By reference to previous studies (8, 12), the Fe-rich phase in the TML is likely siderite ($FeCO_3$). The significant Ca contribution may result either from Fe substitution by Ca in the siderite structure or from an intimate mixing of distinct phases. Assuming Ca in siderite, the mole fraction X_{Ca} = Ca/(Ca + Fe) would equal X_{Ca} = 6.1/(6.1 + 23.7) = 0.20. This ratio is much higher than is thermodynamically stable for Ca-substituted siderite (13). Note also that the O to cation ratio equals 68.1/(6.1 + 23.7 + 1.2) = 2.20, significantly smaller than the ratio of 3 expected for carbonate phases only. However, O quantification by EDX is known to be unreliable.

X-ray diffractograms of the FCP−clay interface revealed the presence of α-iron, quartz, and calcite (Figure SI-4 in the Supporting Information). The detection of quartz and calcite from the clay matrix emphasizes the small width of the corrosion interface compared to that of the micro X-ray beam. A series of XRD peaks systematically located between Bragg peaks of calcite and siderite were also observed and could correspond to a rhombohedral carbonate of structure intermediate between calcite and siderite. To test this hypothesis, these peak positions were Rietveld-refined using GSAS (14) with the crystal structural parameters of siderite as starting values (15). Peak positions are correctly reproduced by this structure (Figure SI-4 in the Supporting Information), and the resulting cell parameters (a_σ = 4.751(3) Å, c_σ = 15.692(12) Å) are systematically bracketed by those of calcite (a_c = 4.9900 Å, c_c = 17.061 Å) and siderite (a_s = 4.6887 Å, c_s = 15.373 Å). If the cell parameters obey the Vegard's law, then X_{Ca} would be obtained simply from the ratio of cell parameters according to X_{Ca} = ($a_\sigma - a_s$)/($a_c - a_s$) = ($c_\sigma - c_s$)/($c_c - c_s$). In the present case, X_{Ca} = 0.21 and 0.19 from a and c parameters, respectively. These values compare well with X_{Ca} derived from the SEM-EDX. Hence, both μXRD and SEM-EDX analyses support the formation of a Ca-doped siderite at the FCP−clay interface.

Anodically Corroded Probe. Corrosion at the APP−clay interface surface was heterogeneously distributed (Figure SI-2 in the Supporting Information). Some areas appeared to be corrosion-free, whereas less than a quarter of the original thickness remained at other points. In addition, layers of
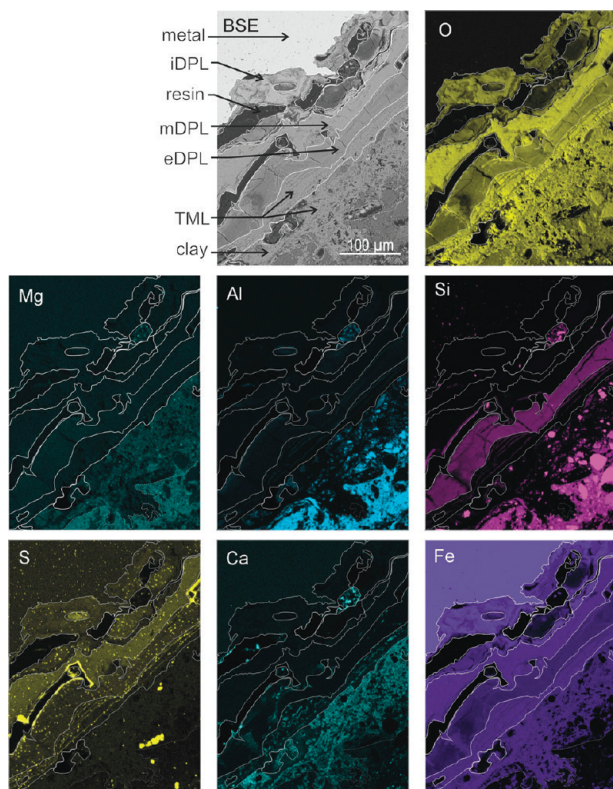
FIGURE 2. Scanning electron microscopy (SEM) by backscattering electrons (BSE) and EDX elemental maps of the APP—clay interface.

corrosion products were often present. In moderately corroded areas, a bright iDPL contacting the metal and a darker eDPL could be observed. In the most extensively corroded areas, DPLs were corrugated and folded, making any layering identification difficult.

The SEM-BSE and SEM-EDX maps of the APP—clay interface correlated the observed layering to dissimilar chemical compositions. For extensively corroded areas, the electron-dense iDPL was present and contained only Fe and O, possibly H and C too (Figure 2). Holes filled with resin perforated the iDPL. In less corroded areas, this iDPL was either absent or restricted to Fe indents. Two additional layers of decreasing electron density could be observed farther from the iron surface. They corresponded to a median DPL (mDPL) containing only Fe and O, possibly with H and C, and an eDPL with Fe, O, Si, and traces of S and Al. All DPL were sometimes jumbled. Finally, the eDPL contacted a TML with (Fe, O)-concentrated areas (Figure 2).

Because of similarities with previous studies (8, 12), we anticipated the bright iDPL to be made of magnetite. Point analyses of the iDPL (points 1 and 2 in Figure SI-5 in the Supporting Information; Table 1) resulted in an atomic O/Fe = 1.22 lower than expected for magnetite (O/Fe = 1.33). Oxidation and/or hydration of the layer would have resulted in O/Fe > 1.33 and, thus, could not account for this discrepancy. This confirmed that O was systematically under-quantified by EDX, hence only relative variations in O content could be compared. Point analyses in the mDPL (points 3, 4, and 7; Table 1) yielded O/Fe ~ 1.75, larger than for magnetite. This larger ratio could result from Fe oxidation or from the formation of hydroxide and/or carbonate compounds. The eDPL (points 5, 6, 8–12) contained only trace amounts of Al, precluding the presence of saponite or chlorite. Additionally, substantial Fe and Si amounts were measured, with a Si/Fe ratio between 0.56 and 0.75. Interestingly, these values compare with the Si/Fe ratio for TO trioctahedral clay minerals ($Fe_3Si_2O_5(OH)_4$, Si/Fe = 0.67).

Finally, EDX analysis of Fe-containing minerals in the TML revealed only Fe and O (possibly H and C), with traces (<1 atomic %) of Ca and other elements, as expected for siderite.

The μRaman spectra of the iDPL (Figure 3) showed three bands at 323, 547, and 676 cm^{-1}, characteristic of magnetite (10, 16). The spectra collected in the mDPL showed a strong Raman band at 1075 cm^{-1} and other bands at 391, 692, 731, and 985 cm^{-1}. These bands are comparable to those observed by Saheb et al. in corroded archeological artifacts (17) and were attributed to an Fe hydroxycarbonate ($FeCO_3(OH)_2$) of chukanovite structure (18). Finally, the Raman spectra for TML displayed bands at 191, 290, and 1093 cm^{-1} typical of carbonate solids. Because these carbonate were shown by SEM-EDX to contain almost only Fe, the only plausible solid is siderite. No specific Raman signal could be obtained for the eDPL, probably because this material was only partially ordered.

The X-ray diffractogram collected for the APP iDPL displayed a significant contribution of magnetite, confirming Raman results (Figure 4a,b). The mDPL diffractograms showed peaks of magnetite, siderite, and chukanovite (18) (Figure 4c,d; see also the discussion on chukanovite identification by XRD in SI). A small peak is also observed near 5°2θ, reflecting the presence of poorly organized 7 Å clay minerals. Finally, TML diffractograms are dominated by siderite and quartz of the clay matrix (Figure 4e,f).

3.3. Estimation of Corrosion Thickness. *Anodically Polarized Probe.* Because the microcontainer initially had a constant thickness, the corroded thickness can be measured as the difference between initial and final thicknesses. To this end, scanning electron micrographs were assembled to visualize the tube section. Then, diameter rays successively inclined by 1° were drawn from the cylinder center, and the tube final thickness measured along each of these 360 rays. The corroded thickness e_{diff} was calculated as the difference between initial and final thicknesses, yielding an average <e_{diff}> = 85 μm, with a dispersion σ_e = 43 μm accounting for the lateral heterogeneity in corrosion. Thus, on average less than 30% of the container initial thickness has been corroded for the investigated APP section, located close to one of the most corroded areas.

The corroded thickness can also be assessed by assuming that oxidized Fe was fully retained in the DPL and TML (8, 9, 19). Hence, the amount of corroded iron can be quantified from Fe present in these layers. This amount is estimated from profiles of Fe concentrations from the metal surface to the argillite matrix, correcting the mass proportion F_x of Fe at each point x of these profiles by the local density ρ_x. Assuming that each layer is homogeneous, an equivalent thickness of corroded metal e_{eq}

$$e_{eq} = \sum d_i F_x \frac{\rho_i}{\rho_{Fe}}$$

was obtained, where ρ_{Fe} is the density of metal Fe, d_i is the layer thickness, and the summation runs over all Fe-containing layers i at the interface. The d_i values were obtained by measuring and averaging the thickness of the corrosion layers at different locations. To simplify, the iDPL, mDPL, eDPL, and TML were considered to be nonporous homogeneous layers of magnetite (ρ_{iDPL} = 5.2), chukanovite (ρ_{mDPL} = 3.6), Fe-phyllosilicate (F_x = 0.44 and ρ_{eDPL} ~ 3.0 (8)), and siderite (ρ_{TML} = 3.87), respectively. For comparison purposes, the indirect method was used only for locations at which the e_{diff} and e_{eq} could be simultaneously and accurately measured. Over 80 individual (e_{diff}, e_{eq}) couples were measured, and the average of e_{diff} and e_{eq} equals <e_{diff}> = 95 μm (σ_e = 73 μm) and <e_{eq}> = 42 μm (σ_e = 28 μm). Since σ_e is not a measure of uncertainty but of the lateral heterogeneity in corroded thickness, <e_{diff}> and <e_{eq}> sig-

TABLE 1. Results of EDX Analyses in the DPL of the APP−clay Interface[a]

	composition (at %)						composition (at. %)				
	O	Fe	Si	S	Al		O	Fe	Si	S	Al
point 01 (iDPL)	54.8	45.2				point 07 (mDPL)	68.1	29.5	1.8	0.1	0.4
point 02 (iDPL)	55.5	44.5				point 08 (eDPL)	46.1	32.2	18.4	1.5	1.8
point 03 (mDPL)	61.7	35.4	1.2	1.7	0.6	point 09 (eDPL)	51.4	27.4	18	1.3	1.8
point 04 (mDPL)	60.9	35.5	1.9	1.7		point 10 (eDPL)	36.5	38.4	21.6	2	1.5
point 05 (eDPL)	45.6	30.9	21.3	1.4	0.8	point 11 (eDPL)	39.5	35.6	21.1	2.3	1.5
point 06 (eDPL)	45.5	31.3	21.8	1.4		point 12 (eDPL)	43.1	29.6	22.3	2.8	2.3

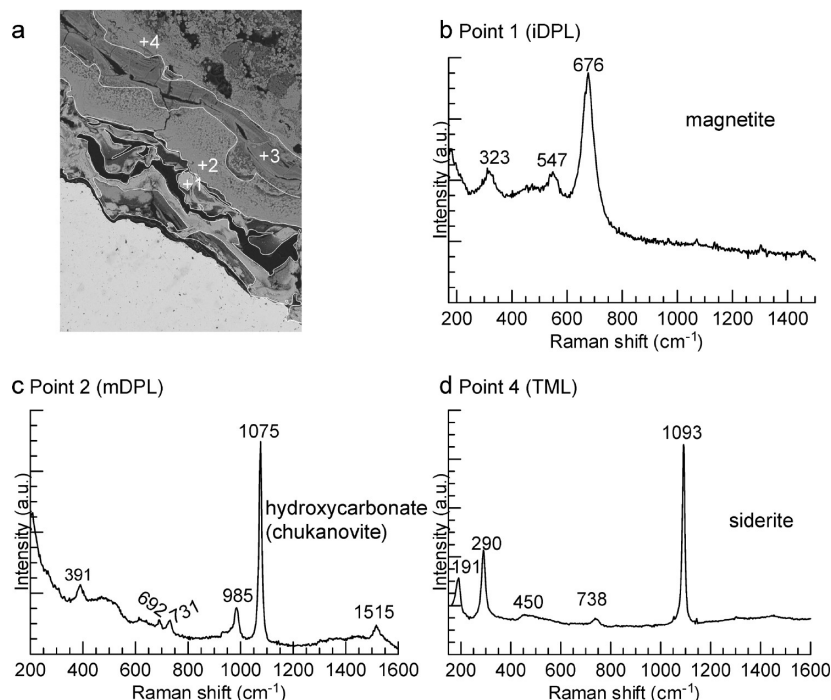[a] The analytical points are marked in Figure SI-5 in the Supporting Information.

FIGURE 3. Raman analysis of the APP−clay interface. (a) Location of the analytical spots. (b) Raman spectrum recorded at point 1 (iDPL). (c) Raman spectrum recorded at point 2 (mDPL). (d) Raman spectrum recorded at point 4 (TML).

nificantly differ, suggesting that e_{eq} somewhat underestimates the corroded thickness. To further investigate this discrepancy, individual e_{eq} were plotted as a function of e_{diff} (Figure SI-7 in the Supporting Information). Most of the points (and all for which $e_{eq} > 40\ \mu$m) lie below the $e_{diff} = e_{eq}$ line. Hence, about 50% of Fe released by corrosion was not retained in the corrosion products. This is in agreement with X-ray tomographic observations showing the presence of dense halos in clay, suggesting migration of oxidized Fe over millimeter distances. Also the comparison of e_{eq} and e_{diff} revealed the limitations of the indirect method to evaluate the corroded thickness, at least for important corrosion under anoxic conditions. Clearly, e_{eq} should be seen at best as a lower estimate of the corroded thickness.

Freely Corroding Probe. The corroded thickness cannot be directly measured on the FCP; hence, the indirect method has been used. However, in some areas where thick layers of resin contacted the DPL, the equivalent thickness from Fe in the TML $e_{eq,TML}$ could not be determined. Assuming that $e_{eq,TML}$ was zero in these areas leads to an average $<e_{eq}> = 5\ \mu$m ($\sigma_e = 3\ \mu$m). Instead, excluding all points for which $e_{eq,TML}$ could not be measured yields $<e_{eq}> = 7\ \mu$m ($\sigma_e = 5\ \mu$m).

4. Discussion
4.1. Corrosion Mechanism at the FCP−Clay Interface.
The observed $e_{eq} \approx 5-7\ \mu$m after 4 months of corrosion at the FCP−clay interface scales with $e_{eq} \approx 14-18\ \mu$m reported for

an iron rod corroded over 8 months in anoxic water-saturated conditions at 90 °C ([8]). Also, the corrosion facies at the FCP−clay interface are similar to that previously observed ([8]). Thus, the corrosion rate and mechanism appear to have been little affected by the possibly high H_2(g) partial pressure (P_{H2}) due to APP activated corrosion. Interestingly, the magnetite iDPL appears to be fragmented and very thin after 4 months. This suggests that this layer develops only after an induction period, as previously observed for Fe spherules corroded in clay slurries ([20]).

Although siderite is observed in all corrosion setups, Ca-doped siderite is rather unexpected, as $CaCO_3$(s) and $FeCO_3$(s) are known to form a very limited solid solution ([13]). At 25 °C, the highest amount of Ca at equilibrium in siderite equals $X_{Ca} < 0.002$, although X_{Ca} values as high as ∼0.085 are expected to be metastable ([13]). Here, $X_{Ca} \sim 0.20$, and the temperature difference from 25 to 90 °C (298 to 363 K) is unlikely to significantly increase X_{Ca} in siderite. Instead, an alternate suggestion is that Ca is kinetically buried in the growing siderite. Later on, decrease in the corrosion rate and recrystallization of Ca-doped siderite to form nearly pure siderite would result in Ca release and transport away from the TML.

4.2. Corrosion at the APP−Clay Interface.
Corrosion was activated at the APP surface, and a thickness of ∼280 μm should have corroded if Fe had been oxidized to the highest possible oxidation state ($Fe^{(III)}$). The actual e_{diff} is a third as
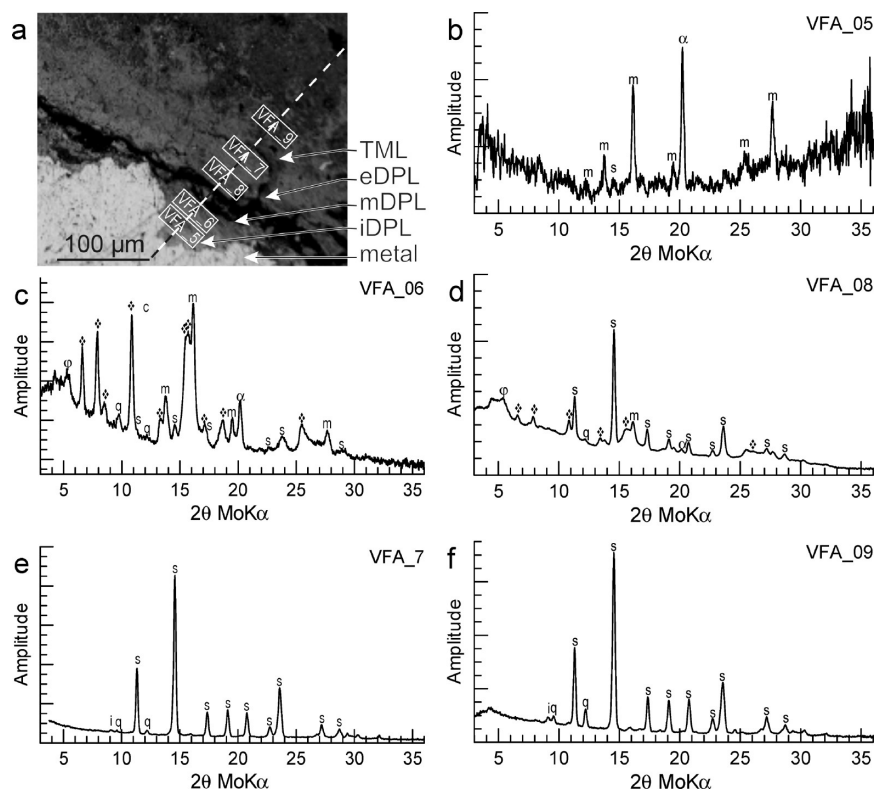
FIGURE 4. (a) Location of micro-XRD diagrams collected at the APP–clay interface. (b–f) Micro X-ray diffractograms collected at the APP–clay interface, in the iDPL (b), mDPL (c), eDPL (d), and TML (f). i: Illite; m: magnetite; q: quartz; s: siderite; α: α-Fe; φ: 7 Å phyllosilicate; diamond: chukanovite.

low, meaning that a parasitic reaction occurred. The most likely reaction is reoxidation of $H_2(g)$ produced by water reduction. This, together with occasional pressure purges from the confining cell, probably prevented P_{H2} from building up. Note however that $H_2(g)$ oxidation should have locally acidified the corrosion interface, which seems at odds with the presence of magnetite and chukanovite. Yet the holes observed in the DPL may also result from localized acid attack. Also, water reduction on the walls of the high-pressure cell would have released hydroxyl anions, and these ions would have set basic conditions in the whole brick, not just the wall–clay interface.

To clarify the preferential formation of chukanovite over siderite, the equilibrium between chukanovite and siderite can be written

$$2 \, FeCO_3 + 2 \, OH^- \leftrightarrow Fe_2CO_3(OH)_2 + CO_3^{2-}$$
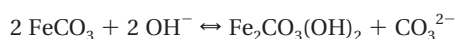
This reaction is controlled only by the CO_2 partial pressure P_{CO2} and by pH. A mildly elevated pH (as evidenced by the presence of magnetite) would favor chukanovite over siderite. Chukanovite formation is also favored by an excess of dissolved Fe[II] (21).

Although corrosion rates for the APP were higher by an order of magnitude than for FCP, the iDPL, eDPL, and TML were somewhat similar in order and mineralogy. Therefore, the precipitation of corrosion products for the two probes appears to be driven by the supply of oxidized Fe, not by precipitation kinetics. Indeed, reactions of precipitation and recrystallization of iron hydroxides, carbonates, and phyllosilicates are known to be rapid at 90 °C (22, 23). A potential effect of greater corrosion rates is that the concentration of dissolved Fe[II] is greater; hence, Fe supersaturation is more important, which would promote the formation of smaller particles, ultimately increasing the reactive surface area. Thus, the chemical reactivity of solids contained in the APP

corrosion layers should be similar to, if not greater than, that of particles formed by free corrosion. Finally, Fe released by corrosion would overwhelm Ca, thus explaining the limited Ca content in siderite near the APP.

4.3. Implications for Nuclear Waste Storage. Whether corrosion was free or anodically activated, the mineralogy of the corrosion products matches the phases observed in previous studies and on archeological artifacts corroded under anoxic conditions (8, 17). The anodic polarization, thus, seems like a valid method to speed up corrosion processes and generate corrosion interfaces in clay. The observed oxidation products have to be considered for a proper modeling of corrosion mechanisms (24). In particular, the short-term formation of siderite at the corrosion interface predicted by modeling is actually observed.

That a significant part of corroded Fe is potentially transported away from the corrosion interface also has significant implications for safety assessment of nuclear waste repositories. Dissolved Fe[II] likely migrates by advection in fractures and diffusion in the clay, where it can be retained in interlayers and on layer edges of clay minerals (25, 26). Edge-sorbed Fe[II] can compete for edge sorption of simple cations, yet it can also promote reduction of reducible species such as selenite (27). In addition, because most of this Fe[II] would not be structural, but dispersed on clay surfaces, it would be entirely available for immediate interaction with solution species. This clearly favors reduction and possibly immobilization of reducible radionuclides.

Supporting Information Available

Supporting Information contains a detailed description of the corrosion setup and of the materials and methods used to prepare and characterize corrosion interfaces. Also, optical microphotographs of the FCP- and AAP-clay interfaces are given, as well as illustrations of microscopic results on the FCP−clay interface (SEM image and chemical maps, X-ray diffractograms). Figure SI-5 compares e_{eq} and e_{diff} values for the APP probe. Rationales for the identification of Ca-doped siderite and chukanovite are supplied too. This material is available free of charge via the Internet at http://pubs.acs.org.

Literature Cited

(1) Féron, D.; Crusset, D.; Gras, J. M. Corrosion issues in nuclear waste disposal. *J. Nucl. Mater.* **2008**, *379*, 16–23.

(2) Madsen, F. T. Clay mineralogical investigations related to nuclear waste disposal. *Clay Min.* **1998**, *33*, 109–129.

(3) Jollivet, P.; Minet, Y.; Nicolas, M.; Vernaz, E. Simulated alteration tests on non-radioactive SON 68 nuclear glass in the presence of corrosion products and environmental materials. *J. Nucl. Mater.* **2000**, *281*, 231–243.

(4) Carlson, L.; Karnland, O.; Oversby, V. M.; Rance, A. P.; Smart, N. R.; Snellman, M.; Vahanen, M.; Werme, L. O. Experimental studies of the interactions between anaerobically corroding iron and bentonite. *Phys. Chem. Earth* **2007**, *32*, 334–345.

(5) Smart, N. R.; Rance, A. P.; Werme, L. O. The effect of radiation on the anaerobic corrosion of steel. *J. Nucl. Mater.* **2008**, *379*, 97–104.

(6) Bataillon, C.; Musy, C.; Roy, M. Corrosion des surconteneurs de déchets, cas d'un surconteneur en acier faiblement allié. *J. Phys. IV* **2001**, *11*, 267–274.

(7) Martin, F. A.; Bataillon, C.; Schlegel, M. L. Corrosion of iron and low alloyed steel within a water saturated brick of clay under anaerobic deep geological disposal conditions: An integrated experiment. *J. Nucl. Mater.* **2008**, *379*, 80–90.

(8) Schlegel, M. L.; Bataillon, C.; Benhamida, K.; Blanc, C.; Menut, D.; Lacour, J.-L. Metal corrosion and argillite transformation at the water-saturated, high temperature iron-clay interface: a microscopic-scale study. *Appl. Geochem.* **2008**, *23*, 2619–2633.

(9) Chitty, W. J.; Dillmann, P.; L'Hostis, V.; Lombard, C. Long-term corrosion resistance of metallic reinforcements in concrete - a study of corrosion mechanisms based on archaeological artefacts. *Corros. Sci.* **2005**, *47*, 1555–1581.

(10) Neff, D. Apport des analogues archéologiques à l'estimation des vitesses moyennes et à l'étude des mécanismes de corrosion à très long terme des aciers non alliés dans les sols; Université de Technologie: Compiègne, France, 2003.

(11) Hammersley, A. P. *FIT2D reference manual*; ESRF: Grenoble, France, 1993.

(12) Neff, D.; Dillmann, P.; Bellot-Gurlet, L.; Berranger, G. Corrosion of iron archaeological artefacts in soil: characterisation of the corrosion system. *Corros. Sci.* **2005**, *47*, 515–535.

(13) Lippmann, F. Phase diagrams depicting aqueous solubility of binary mineral systems. *Neues Jahrb. Mineral., Abh.* **1980**, *139*, 1–25.

(14) Larson, A. C.; Von Dreele, R. B. *General Structure Analysis System (GSAS)*; Los Alamos National Laboratory: Los Alamos, New Mexico, 2000.

(15) Effenberger, H.; Mereiter, K.; Zemann, J. Crystal-structure refinements of magnesite, calcite, rhodochrosite, siderite, smithonite, and dolomite, with discussion of some aspects of the stereochemistry of calcite type carbonates. *Z. Kristallogr.* **1981**, *156*, 233–243.

(16) Dunn, D. S.; Bogart, M. B.; Brossia, C. S.; Cragnolino, G. A. Corrosion of iron under alternating wet and dry conditions. *Corrosion* **2000**, *56*, 470–481.

(17) Saheb, M.; Neff, D.; Dillmann, P.; Matthiesen, H.; Foy, E. Long-term corrosion behaviour of low-carbon steel in anoxic environment: characterization of archaeological artefacts. *J. Nucl. Mater.* **2008**, *379*, 118–123.

(18) Pekov, I. V.; Perchiazzi, N.; Merlino, S.; Vyacheslav, N.; Merlini, M.; Zadov, A. E. Chukanovite, $Fe_2(CO_3)(OH)_2$, a new mineral from the weathered iron meteorite Dronino. *Eur. J. Mineral.* **2007**, *19*, 891–898.

(19) Neff, D.; Bellot-Gurlet, L.; Dillmann, P.; Reguer, S.; Legrand, L. Raman imaging of ancient rust scales on archaeological iron artefacts for long-term atmospheric corrosion mechanisms study. *J. Raman Spectrosc.* **2006**, *37*, 1228–1237.

(20) de Combarieu, G.; Barboux, P.; Minet, Y. Iron corrosion in Callovo-Oxfordian argilite: From experiments to thermodynamic/kinetic modelling. *Phys. Chem. Earth* **2007**, *32*, 346–358.

(21) Remazeilles, C.; Refait, P. Fe(II) hydroxycarbonate $Fe_2(OH)_2CO_3$ (chukanovite) as iron corrosion product: Synthesis and study by Fourier Transform Infrared Spectroscopy. *Polyhedron* **2009**, *28*, 749–756.

(22) Decarreau, A. Partitioning of divalent transition elements between octahedral sheets of trioctahedral smectites and water. *Geochim. Cosmochim. Acta* **1985**, *49*, 1537–1544.

(23) Schwertmann, U.; Cornell, R. M. *Iron oxides in the laboratory*; VCH verlag: Weinheim, Germany, 1991.

(24) Bildstein, O.; Trotignon, L.; Perronnet, M.; Jullien, M. Modelling iron-clay interactions in deep geological disposal conditions. *Phys. Chem. Earth* **2006**, *31*, 618–625.

(25) Tournassat, C.; Lerouge, C.; Blanc, P.; Brendlé, J.; Greneche, J. M.; Touzelet, S.; Gaucher, E. C. Cation exchanged Fe(II) and Sr compared to other divalent cations (Ca, Mg) in the bure Callovian-Oxfordian formation: Implications for porewater composition modelling. *Appl. Geochem.* **2008**, *23*, 641–654.

(26) Schlegel, M. L.; Manceau, A. Evidence for the nucleation and epitaxial growth of Zn phyllosilicate on montmorillonite. *Geochim. Cosmochim. Acta* **2006**, *70*, 901–917.

(27) Charlet, L.; Scheinost, A. C.; Tournassat, C.; Greneche, J. M.; Géhin, A.; Fernandez-Martinez, A.; Coudert, S.; Tisserand, D.; Brendle, J. Electron transfer at the mineral/water interface: Selenium reduction by ferrous iron sorbed on clay. *Geochim. Cosmochim. Acta* **2007**, *71*, 5731–5749.